

Retinal lipid and glucose metabolism dictates angiogenesis through the lipid sensor Ffar1

Jean-Sébastien Joyal^{1–3}, Ye Sun⁴, Marin L Gantner⁵, Zhuo Shao⁴, Lucy P Evans⁴, Nicholas Saba⁴, Thomas Fredrick⁴, Samuel Burnim⁴, Jin Sung Kim³, Gauri Patel², Aimee M Juan⁴, Christian G Hurst⁴, Colman J Hatton⁴, Zhenghao Cui⁴, Kerry A Pierce⁶, Patrick Bherer⁷, Edith Aguilar⁸, Michael B Powner⁹, Kristis Vevis⁹, Michel Boisvert¹⁰, Zhongjie Fu⁴, Emile Levy¹⁰, Marcus Fruttiger⁹, Alan Packard¹¹, Flavio A Rezende¹², Bruno Maranda⁷, Przemyslaw Sapielha¹², Jing Chen⁴, Martin Friedlander⁸, Clary B Clish⁶ & Lois E H Smith⁴

Tissues with high metabolic rates often use lipids, as well as glucose, for energy, conferring a survival advantage during feast and famine¹. Current dogma suggests that high-energy-consuming photoreceptors depend on glucose^{2,3}. Here we show that the retina also uses fatty acid β -oxidation for energy. Moreover, we identify a lipid sensor, free fatty acid receptor 1 (Ffar1), that curbs glucose uptake when fatty acids are available. Very-low-density lipoprotein receptor (Vldlr), which is present in photoreceptors⁴ and is expressed in other tissues with a high metabolic rate, facilitates the uptake of triglyceride-derived fatty acid^{5,6}. In the retinas of *Vldlr*^{-/-} mice with low fatty acid uptake⁶ but high circulating lipid levels, we found that Ffar1 suppresses expression of the glucose transporter Glut1. Impaired glucose entry into photoreceptors results in a dual (lipid and glucose) fuel shortage and a reduction in the levels of the Krebs cycle intermediate α -ketoglutarate (α -KG). Low α -KG levels promotes stabilization of hypoxia-induced factor 1a (Hif1a) and secretion of vascular endothelial growth factor A (Vegfa) by starved *Vldlr*^{-/-} photoreceptors, leading to neovascularization. The aberrant vessels in the *Vldlr*^{-/-} retinas, which invade normally avascular photoreceptors, are reminiscent of the vascular defects in retinal angiomatous proliferation, a subset of neovascular age-related macular degeneration (AMD)⁷, which is associated with high vitreous VEGFA levels in humans. Dysregulated lipid and glucose photoreceptor energy metabolism may therefore be a driving force in macular telangiectasia, neovascular AMD and other retinal diseases.

Retinal angiomatous proliferation (RAP) is observed in macular telangiectasia (MacTel)⁸, as well as in 15–20% of cases of neovascular AMD⁷, the leading cause of blindness in older adults⁹. Photoreceptors, which are densest in the macula, are among the highest energy-consuming and mitochondria-rich cell types^{2,10}, suggesting the hypothesis that insufficient energy production for the high-energy demands of photoreceptors contributes to macular neovascularization. VEGFA contributes to retinal neovascularization, but factors that initiate VEGFA secretion in macular disease remain mostly unknown. We hypothesized that disordered photoreceptor mitochondrial energy metabolism might drive aberrant angiogenesis in the normally avascular photoreceptors in an attempt to increase fuel supply, consistent with the observation that dyslipidemia and mitochondrial dysfunction (which are associated with aging) are important risk factors for neovascular AMD⁹.

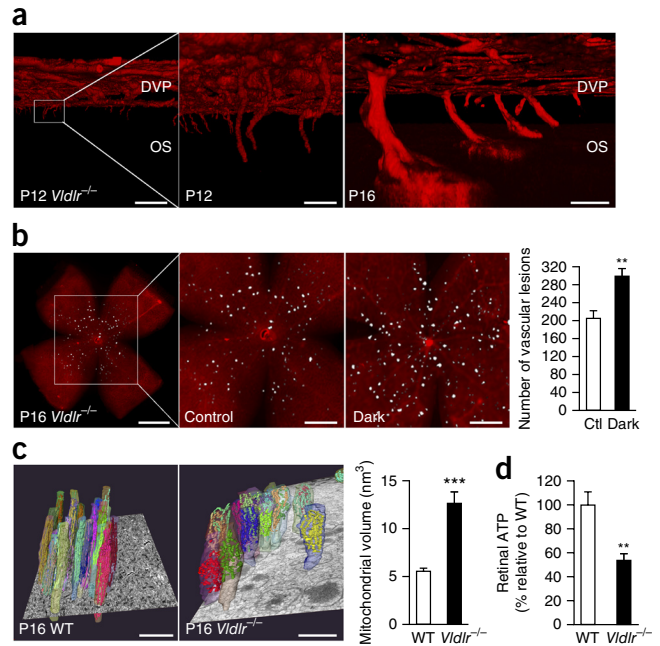
Retinal neurons are thought to rely on glucose for fuel^{2,3}. Glucose is metabolized to pyruvate (by glycolysis) and either converted to lactate in the cytoplasm or oxidized to acetyl-coenzyme A (acetyl-CoA) in mitochondria before entering the Krebs cycle to produce ATP. In photoreceptors, the major glucose transporter is solute carrier family 2 (facilitated glucose transporter), member 1 (Slc2a1; also known as Glut1)^{11,12}. Clinically, *SLC2A1* (hereafter referred to as *GLUT1*) deficiency causes infantile seizures and developmental delay¹³, highlighting the importance of glucose metabolism in the brain. However, *GLUT1*-deficient individuals have normal vision, suggesting the use of alternative retinal energy substrates, perhaps through lipid β -oxidation.

Lipid β -oxidation commonly occurs in the heart and skeletal muscle (tissues with high metabolic rates), where abundant amounts

¹Department of Pediatrics, Centre Hospitalier Universitaire (CHU) Sainte-Justine Research Center, Université de Montréal, Montreal, Quebec, Canada. ²Department of Pharmacology, Université de Montréal, Montreal, Quebec, Canada. ³Department of Pharmacology and Therapeutics, McGill University, Montreal, Quebec, Canada. ⁴Department of Ophthalmology, Harvard Medical School, Boston Children's Hospital, Boston, Massachusetts, USA. ⁵Lowy Medical Research Institute, La Jolla, California, USA. ⁶Metabolite Profiling Platform, The Broad Institute of the Massachusetts Institute of Technology (MIT) and Harvard University, Cambridge, Massachusetts, USA. ⁷Department of Genetics, Université de Sherbrooke, Sherbrooke, Quebec, Canada. ⁸Department of Cell and Molecular Biology, Scripps Research Institute, La Jolla, California, USA. ⁹Institute of Ophthalmology, University College London, London, UK. ¹⁰Department of Nutrition, Centre Hospitalier Universitaire (CHU) Sainte-Justine Research Center, Université de Montréal, Montreal, Quebec, Canada. ¹¹Department of Radiology, Harvard Medical School, Boston Children's Hospital, Boston, Massachusetts, USA. ¹²Department of Ophthalmology, Maisonneuve-Rosemont Hospital Research Centre, Université de Montréal, Montreal, Quebec, Canada. Correspondence should be addressed to L.E.H.S. (lois.smith@childrens.harvard.edu) or J.-S.J. (js.joyal@umontreal.ca).

Received 10 October 2015; accepted 5 February 2016; published online 14 March 2016; doi:10.1038/nm.4059

Figure 1 Retinal energy deficits are associated with vascular lesions in *Vldlr*^{-/-} mice. **(a)** Representative (of $n = 5$ retinas) flat-mount 3D reconstruction of confocal microscopy images of retinas from a P12 (left and middle) and a P16 (right) *Vldlr*^{-/-} mouse, focusing on blood vessels (stained red with Simplifonica B4 isolectin) in the photoreceptor layer. At P12, pathologic vessels in *Vldlr*^{-/-} retinas originated from the deep vascular plexus (DVP) and breached the outer plexiform layer; at P16, the vessels extended toward photoreceptor outer segments (OS). Scale bars, 500 μm (left) and 100 μm (middle and right). **(b)** Left, representative flat-mount images of retinas, imaged by focusing on the photoreceptor layer, from P16 *Vldlr*^{-/-} pups that were raised with a normal 12-h light and 12-h dark cycle (control) or in darkness (dark). Pathological RAP-like vessels were pseudo-colored in white for quantification; the boxed area is enlarged in the middle micrographs. The graph shows the number of vascular lesions in retinas from P16 *Vldlr*^{-/-} pups that were raised in control conditions (Ctl; $n = 28$ retinas) or in darkness ($n = 10$ retinas). Scale bars, 1 mm (left) and 0.5 mm (middle and right). $P = 0.0031$. **(c)** Representative 3D-reconstructed scanning electron microscopy (SEM) images of retinas from P16 WT (left) and *Vldlr*^{-/-} (middle) mice and quantification of photoreceptor mitochondrial volume (right) ($n = 23$ photoreceptors per group). Mitochondria within photoreceptors are pseudo-colored. Scale bars, 5 μm . **(d)** ATP levels in retinas from P16 *Vldlr*^{-/-} ($n = 6$) and WT littermate control ($n = 4$) mice. $P = 0.0026$. In all graphs, results are presented as mean \pm s.e.m. ** $P < 0.01$, *** $P < 0.001$; by two-tailed Student's *t*-test.



of VLDLR facilitate fatty acid uptake¹⁴. VLDLR binds chylomicrons and enables cleavage of long-chain fatty acids from triglycerides by lipoprotein lipase⁶. *Vldlr* is involved in the transcytosis of active lipoprotein lipase across endothelial cells¹⁵, enabling the delivery of free fatty acid to tissue. *Vldlr* contributes to lipid uptake and fatty acid β -oxidation in the heart⁵. Because lipid β -oxidation enzymes are expressed in the eye¹⁶, we hypothesized that fatty acid β -oxidation is used for energy in lipid- and *Vldlr*-rich photoreceptors. *VLDLR* deletion causes maculopathy in humans¹⁷, and *Vldlr*^{-/-} mice develop RAP-like retinal vascular lesions (Fig. 1a)⁴. Study of *Vldlr*^{-/-} mice thus allows for the exploration of the hypotheses that lipids fuel photoreceptors and that fuel deficiency promotes neovessel formation.

We first tested whether there was a link between the number of RAP-like lesions and photoreceptor energy demand. Rod photoreceptors consume 3–4 times more energy in darkness than in light to maintain the ‘dark current’, an electrochemical gradient required for photon-induced depolarization¹⁰. Conversely, membrane turnover and visual cycle activity are decreased in darkness¹⁰. Dark-raised *Vldlr*^{-/-} mice developed 1.5-fold more RAP-like vascular lesions than light and dark cycle–raised mice (Fig. 1b), suggesting that energy metabolism influences neovascular disease. Photoreceptors mature from the optic nerve outward toward the periphery, and energy consumption increases as photoreceptors mature^{2,18}. In retinas from postnatal day 16 (P16) *Vldlr*^{-/-} mice, the more mature central retina had more RAP-like lesions than the peripheral retina (Fig. 1b), consistent with this model.

To determine whether loss of *Vldlr* specifically in photoreceptors is sufficient to drive pathological vessel formation, we knocked down expression of *Vldlr* in the photoreceptors of *Vldlr*^{+/-} mice, which have normal circulating fatty acid levels and do not have a RAP-like phenotype¹⁹. To knock down *Vldlr* expression selectively in photoreceptors, we used an adeno-associated virus (AAV) 2–derived hRK construct, which contains a photoreceptor-specific human rhodopsin kinase gene (*GRK1*) promoter driving the expression of shRNA that targets *Vldlr* expression. Loss of *Vldlr* expression in photoreceptors led to the development of RAP-like lesions (Supplementary Fig. 1).

Consistent with the concept that *Vldlr*^{-/-} photoreceptors are energy deficient, they had swollen mitochondria, as assessed by three-dimensional (3D) scanning electron microscopy (Fig. 1c and Supplementary Videos 1 and 2). Moreover, retinas from *Vldlr*^{-/-} mice had reduced ATP stores (Fig. 1d), confirming an energy deficit.

To explore the mechanistic basis of the photoreceptor energy deficit, we examined the contribution of fatty acids and glucose to energy production in wild-type (WT) retinas (Supplementary Fig. 2a). The long-chain fatty acid palmitate fueled mitochondrial β -oxidation in retinal explants, doubling the oxygen-consumption rate (OCR); moreover, treatment with etomoxir, which inhibits fatty acid transport into mitochondria, abrogated palmitate-induced mitochondrial respiration, confirming that fatty acid β -oxidation contributes to retinal energy metabolism (Fig. 2a,b and Supplementary Fig. 2a–c). We also examined the contribution of glucose oxidation and found that retinal glucose could be oxidized by mitochondria as efficiently as a fatty acid (Supplementary Fig. 2d–f). However, as reported by Warburg, Cohen and Winkler^{3,20}, the vast majority of glucose (87%) was converted to lactate by glycolysis rather than being used for oxidative phosphorylation (Supplementary Fig. 2g). Unlike retinas from WT mice, those from *Vldlr*^{-/-} mice (i.e., with limited fatty acid uptake) did not increase mitochondrial respiration after exposure to palmitate (Supplementary Fig. 2h). Therefore, in addition to glucose, fatty acids contribute to retinal energy production, which may be deficient in retinas from *Vldlr*^{-/-} mice.

Given the possible role of VLDLR in retinal lipid energy metabolism, we quantified retinal fatty acid uptake. Consistent with a previous report²¹, *Vldlr* was highly expressed in retinal photoreceptors (Supplementary Fig. 3a), and uptake of long-chain fatty acids was reduced in retinas from *Vldlr*^{-/-} mice (Supplementary Fig. 3b,c). Serum turbidity reflected higher circulating lipid levels in *Vldlr*^{-/-} versus WT mice (Supplementary Fig. 3b,c). Plasma levels of triglycerides and medium- and long-chain fatty acids (particularly palmitate) were elevated in *Vldlr*^{-/-} mice as compared to WT mice (Fig. 2c and Supplementary Fig. 3d,e). Notably, fatty acid β -oxidation of lipids to produce acetyl-CoA in mitochondria was suppressed in retinas from *Vldlr*^{-/-} mice (Fig. 2d), and total

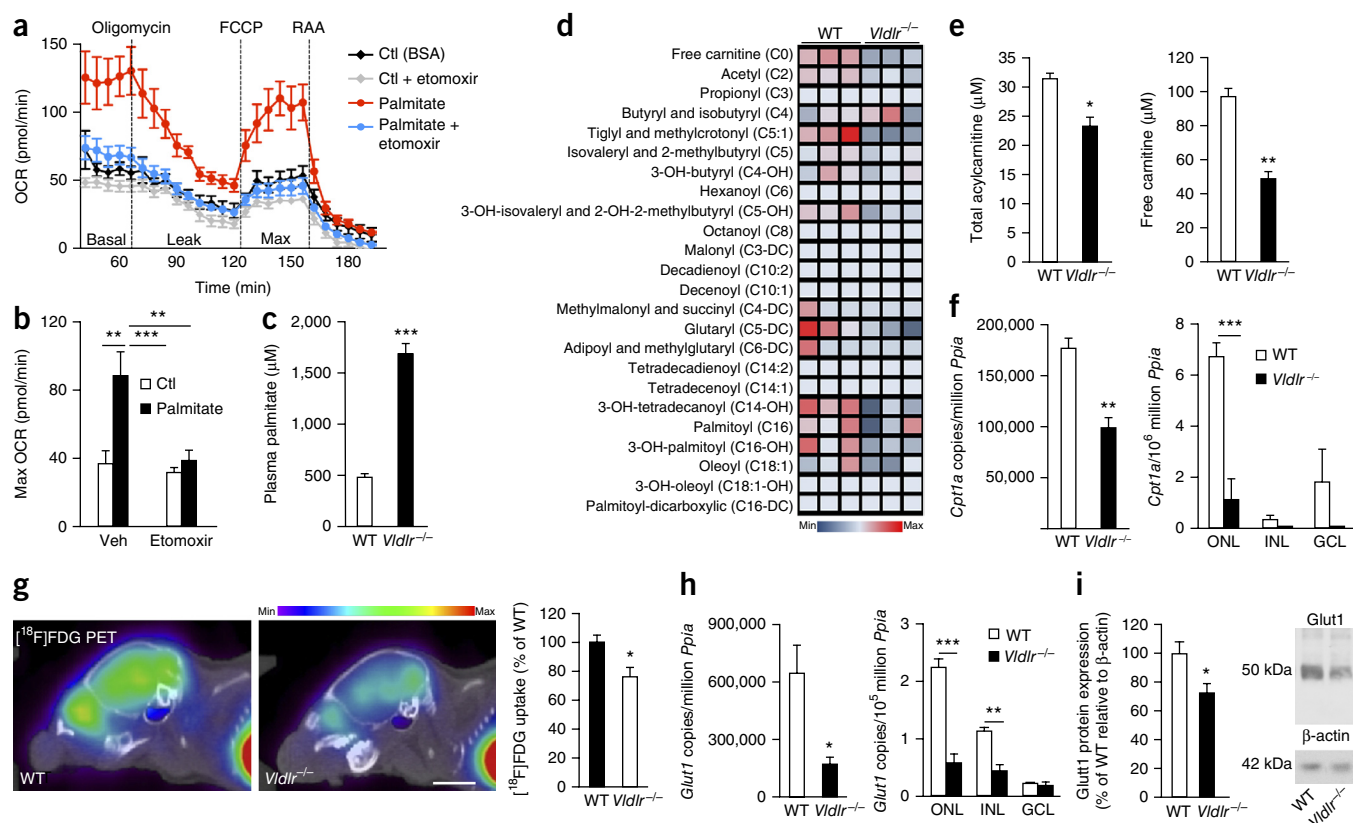


Figure 2 Dual lipid and glucose fuel deficiency in *Vidlr*^{-/-} retinas. **(a,b)** OCR **(a)** and calculated maximal OCR **(b)** of WT retinas treated with the long-chain fatty acid palmitate or BSA (Ctl) in the presence of a DMSO control (Veh) or etomoxir (40 μ M) (number of retinas evaluated: Ctl, $n = 7$; Ctl + etomoxir, $n = 7$; palmitate, $n = 6$; palmitate + etomoxir, $n = 8$). Basal indicates initial OCR without treatment; leak indicates OCR independent of ATP production, after addition of oligomycin to induce a proton leak; max indicates maximal OCR, after addition of FCCP (carbonyl cyanide-*p*-trifluoromethoxyphenylhydrazone). Treatment with rotenone + antimycin A (RAA) reveals nonmitochondrial respiration. **(c)** Circulating levels of palmitate in the plasma of WT ($n = 7$) and *Vidlr*^{-/-} ($n = 13$) mice. **(d)** Metabolite array to assess the levels of fatty acid β -oxidation metabolites in the retinas of WT and *Vidlr*^{-/-} mice ($n = 3$ mice per group; each column represents one mouse retina). **(e)** Total amounts of acylcarnitine ($P = 0.0108$) (left) and levels of free carnitine ($P = 0.0014$) (right) in retinas from WT and *Vidlr*^{-/-} mice, as measured by LC-MS/MS ($n = 3$ retinas per group). **(f)** qRT-PCR analysis for *Cpt1a* expression in intact WT and *Vidlr*^{-/-} retinas ($P = 0.0052$) (left) and in retinal layers after laser-capture microdissection (LCM) (right) ($n = 3$ retinas per group). ONL, outer nuclear layer (photoreceptors); INL, inner nuclear layer; GCL, ganglion cell layer. **(g)** Representative [¹⁸F]FDG microPET and computed tomography images of retinas from WT (left) and *Vidlr*^{-/-} (middle) mice and quantification of [¹⁸F]FDG uptake (right) (WT, $n = 22$; *Vidlr*^{-/-}, $n = 12$ retinas; $P = 0.0116$). The color bar represents the range of [¹⁸F]FDG uptake from minimum (blue) to maximum (red) uptake. Scale bar, 4 mm. **(h)** qRT-PCR analysis for *Slc2a1* (*Glut1*) expression in intact retinas (WT, $n = 9$; *Vidlr*^{-/-}, $n = 12$; $P = 0.0119$) (left) or in retinal layers after LCM ($n = 3$ retinas per group) (right). **(i)** Quantification of Glut1 protein expression in intact retinas from WT and *Vidlr*^{-/-} mice ($n = 6$ retinas per group; $P = 0.030$) (left) from immunoblots (representative blots shown on right). Throughout, results are presented as mean \pm s.e.m. * $P < 0.05$, ** $P < 0.01$, *** $P < 0.001$; by two-tailed Student's *t*-test (**c–f**, **g–i**) or one-way analysis of variance (ANOVA) with Tukey *post hoc* analysis (**b,f,h**).

acylcarnitine levels, as well as free carnitine levels, were reduced (**Fig. 2e**). Low cytosolic fatty acid levels in the retinas from *Vidlr*^{-/-} mice were associated with decreased peroxisome proliferator activated receptor alpha (*Ppara*) mRNA expression²², mainly in the photoreceptors (**Supplementary Fig. 4a,b**). PPARA is a key regulator of several steps of fatty acid β -oxidation²² and regulates expression of carnitine palmitoyl transferase 1a (*Cpt1a*), an enzyme that mediates internalization of fatty acids into mitochondria (**Supplementary Fig. 2a**). Consistent with the effects observed for *Ppara* expression, *Cpt1a* mRNA expression was lower in photoreceptors from *Vidlr*^{-/-} mice than in those from WT mice (**Fig. 2f**). Retinas from *Vidlr*^{-/-} mice that had been treated with the selective *Ppara* agonist WY16463, which is used to enhance fatty acid β -oxidation²³, showed reduced numbers of RAP-like lesions (**Supplementary Fig. 4c**). Treatment of photoreceptor cells (661W cells) with palmitate increased mitochondrial respiration by fatty acid β -oxidation, and this was further increased by addition of the *Ppara* agonist GW9578; this effect was

dependent on fatty acid β -oxidation, because treatment with etomoxir abrogated the increase in mitochondrial respiration (**Supplementary Fig. 5a–d**). Extracellular acidification rates, which reflect lactate production from glycolysis, were not affected by *Ppara* agonist treatment (**Supplementary Fig. 5e,f**). Our findings therefore suggest that fatty acids are an energy substrate in retina and cultured photoreceptors.

We initially anticipated that a compensatory upsurge in glucose uptake would occur to mitigate fatty acid deficiency in *Vidlr*^{-/-} retinas. However, glucose uptake assessed using the radiolabeled glucose analogue [¹⁸F]FDG, as visualized by positron-emitting tomography (PET) and measured by gamma counts, was reduced in retinas from *Vidlr*^{-/-} mice as compared to those from WT mice (**Fig. 2g** and **Supplementary Video 3**); *Glut1* expression was also reduced (**Fig. 2h,i**), particularly in *Vidlr*^{-/-} photoreceptors (**Fig. 2h**). Consistent with these results, carbohydrate metabolism was the most significantly regulated pathway observed in gene microarray data comparing WT to *Vidlr*^{-/-} retinas (**Supplementary Fig. 6a**). Decreased expression

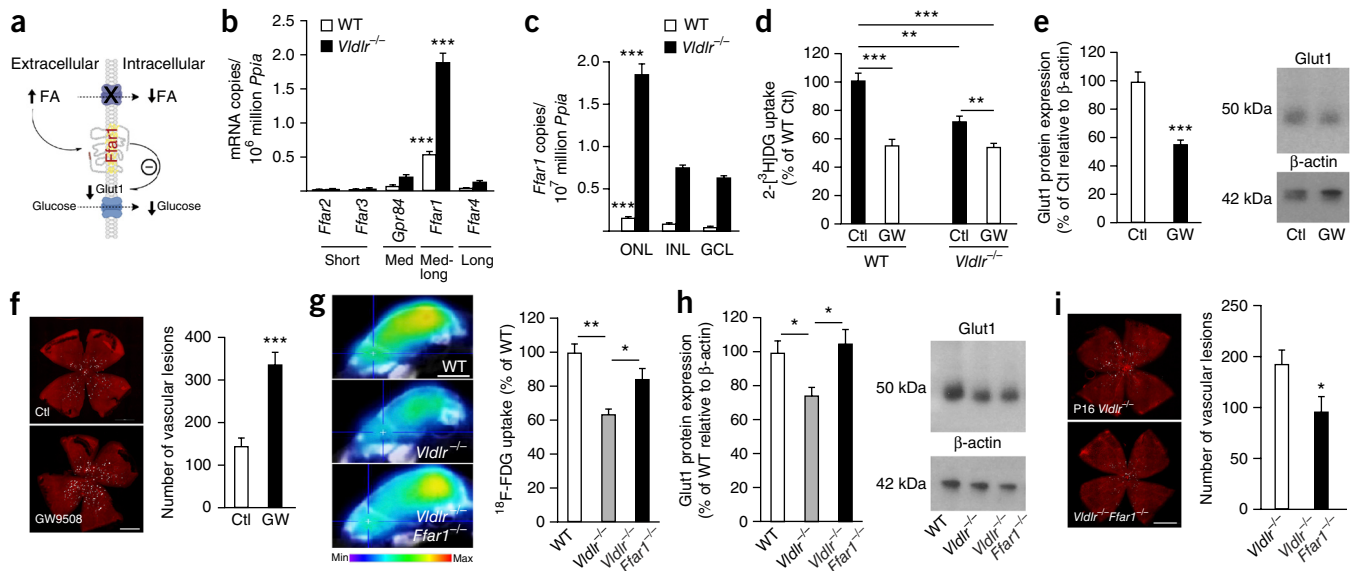


Figure 3 Ffar1 modulates retinal glucose uptake and RAP. (a) Schematic showing that decreased lipid uptake in *Vldlr*^{-/-} retinas results in increased levels of extracellular medium- and long-chain fatty acids. These increased levels are sensed by the GPCR Ffar1 and lead to suppression of Glut1 expression and glucose uptake. (b) qRT-PCR analysis for genes encoding GPCRs involved in sensing short-chain (*Ffar2* and *Ffar3*), medium-chain (med; *Gpr84*), medium- to long-chain (med-long; *Ffar1*) or long-chain (*Ffar4*) fatty acids in intact retinas from WT and *Vldlr*^{-/-} mice ($n = 3$ retinas per group). (c) Distribution of *Ffar1* mRNA in retinal layers ($n = 3$ retinas per group). (d) Glucose uptake in the retinas of WT and *Vldlr*^{-/-} mice treated with vehicle control (Ctl; ethanol) or the Ffar1 agonist GW9508 (GW), as assessed by using a 2-³HJDG tracer (number of retinas evaluated: WT Ctl, $n = 5$; WT GW, $n = 8$; *Vldlr*^{-/-} Ctl, $n = 9$; *Vldlr*^{-/-} GW, $n = 16$). (e) Quantification of Glut1 protein expression in retinas from P16 WT and *Vldlr*^{-/-} mice after treatment with vehicle (Ctl) or GW9508 (GW) ($n = 12$ retinas per group) (left) from immunoblots (representative blots shown on right). (f) Representative images (top and bottom) and quantification (right) of RAP-like pathologic vascular lesions in vehicle-treated (Ctl; $n = 7$ retinas) or GW9508-treated (GW; $n = 11$ retinas) retinas from P16 *Vldlr*^{-/-} mice ($P = 0.0002$). Scale bar, 1 mm. (g–i) Analysis of P16 WT, *Vldlr*^{-/-} and littermate *Vldlr*^{-/-}*Ffar1*^{-/-} mice for [¹⁸F]FDG uptake (representative images (g, left) and quantification (g, right); $n = 4$ retinas per group) (g), Glut1 protein expression (representative immunoblots (h, right) and quantification (h, left); WT, $n = 10$ retinas; *Vldlr*^{-/-}, $n = 9$ retinas; *Vldlr*^{-/-}*Ffar1*^{-/-}, $n = 9$ retinas) and RAP-like pathologic vascular lesions (representative images for *Vldlr*^{-/-} (i, top) and *Vldlr*^{-/-}*Ffar1*^{-/-} (i, bottom) retinas and quantification (i, right); $n = 10$ retinas per group; $P = 0.0153$) (i). In i, WT mice had no vascular lesions. Results are presented as mean \pm s.e.m. * $P < 0.05$, ** $P < 0.01$, *** $P < 0.001$; by two-tailed Student's *t*-test (e,f,i) or one-way ANOVA with Dunnett's (b,c,g,h) or Tukey's (d) *post hoc* comparison. Color bar in g represents the range of [¹⁸F]FDG uptake from minimum (blue) to maximum (red) uptake. Scale bars, 4 mm (g) and 1 mm (i).

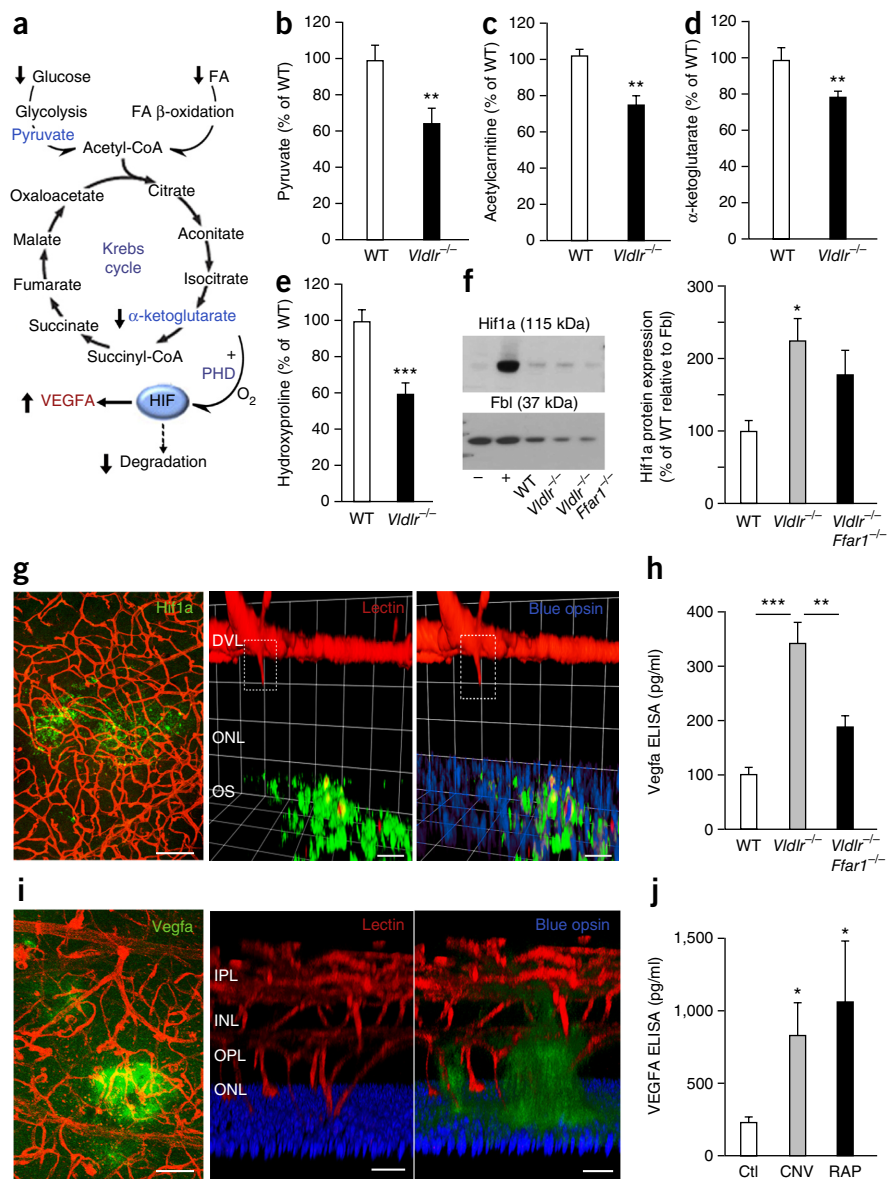
of the gene encoding pyruvate kinase (*Pkm*), which is a critical enzyme in glycolysis, was observed in *Vldlr*^{-/-} retinas in the microarray experiment and confirmed by qRT-PCR (Supplementary Fig. 6b). Expression of the Slc2a3 (Glut3) and Slc2a4 (Glut4) proteins was not affected (Supplementary Fig. 6c). Hence, *Vldlr*^{-/-} retinas display both lipid- and glucose-uptake defects, consistent with a generalized energy shortage.

We posited that despite the lipid-uptake deficiency in *Vldlr*^{-/-} retinas, the increased abundance of lipids in serum from *Vldlr*^{-/-} mice might signal through lipid sensors to reduce glucose uptake, as a means to control fuel supply to the retina (Fig. 3a). Of the known fatty acid-sensing G protein-coupled membrane receptors (GPCRs) we screened in WT retinas, Ffar1 was the most abundantly expressed, and its expression level was increased further in retinas from *Vldlr*^{-/-} mice, particularly in photoreceptors (Fig. 3b,c). Ffar1, first discovered in the pancreas²⁴, governs glucose transport and insulin secretion in pancreatic islet beta cells^{25,26}. High expression of Ffar1 in the pancreas suppresses expression of Slc2a2 (Glut2), the main endocrine pancreas glucose transporter²⁷. Ffar1 has also been localized in the brain, where its function is not well characterized^{28,29}. In WT and *Vldlr*^{-/-} retinas, we found that treatment with a Ffar1 agonist (GW9508) suppressed expression of Glut1 (ref. 12) and retinal glucose uptake (Fig. 3d,e and Supplementary Fig. 7a). Notably, treatment of *Vldlr*^{-/-} mice with GW9508 more than doubled the number of RAP-like lesions, as compared to those in untreated controls (Fig. 3f). Ffar1 binds lipids that

contain >6 carbon atoms²⁹. *Vldlr*^{-/-} mice treated with medium-chain triglycerides (MCT; 8–10 carbon atoms), which are Ffar1 agonists²⁹, or with the Ffar1-selective agonist TAK-875 (ref. 30) had a further decrease in the level of retinal *Glut1* expression and more RAP-like lesions, as compared to untreated controls (Supplementary Fig. 8). Next we generated mice that were deficient in both *Vldlr* and *Ffar1*. Retinas from *Vldlr*^{-/-}*Ffar1*^{-/-} mice had increased glucose uptake and increased *Glut1* expression at the mRNA and protein levels, as compared to those from *Vldlr*^{-/-} mice (Fig. 3g,h, Supplementary Fig. 7b,c and Supplementary Video 3). *Vldlr*^{-/-}*Ffar1*^{-/-} mice also had fewer RAP-like lesions than *Vldlr*^{-/-} mice (Fig. 3i). *In vitro*, knockdown of *Ffar1* or treatment with the mitogen-activated protein kinase (MAPK) kinase inhibitor PD98059 prevented the suppression of *Glut1* expression by GW9508 treatment in 661W photoreceptor cells (Supplementary Fig. 7d–f). Therefore, Ffar1 may act as nutrient sensor, coupling mitochondrial metabolism with the availability of circulating substrates.

We hypothesized that photoreceptors challenged by a deficiency of both glucose and lipid substrates would signal to increase vascular supply in an attempt to restore energy homeostasis (Fig. 4a). Hypoxia has been assumed to be the main driver of angiogenesis, but inadequate nutrient availability to tissue might also control blood vessel growth. As compared to WT retinas, *Vldlr*^{-/-} retinas had reduced levels of pyruvate (a metabolic intermediate that feeds into the Krebs cycle), acetylcarnitine (which provides an estimation of acetyl-CoA

Figure 4 Fuel-deficient *Vldlr*^{-/-} retinas generate less α -KG and more Vegfa. (a) In *Vldlr*^{-/-} retinas, a shortage of both glucose uptake and fatty acid uptake is anticipated to reduce the amount of acetyl-CoA entering the Krebs cycle and the levels of the metabolite intermediate α -KG. Together with oxygen (O_2), α -KG is an essential co-activator of prolyl-hydroxylase dehydrogenase (PHD) that tags Hif1 α for degradation by proline hydroxylation (hydroxyproline). Hif1 α is a transcription factor that promotes the expression of VEGFA. (b–e) Quantification of pyruvate (WT, $n = 15$ retinas; *Vldlr*^{-/-}, $n = 12$ retinas; $P = 0.0032$) (b), acetylcarnitine ($n = 3$ retinas per group; $P = 0.0094$) (c), α -KG (WT, $n = 11$ retinas; *Vldlr*^{-/-}, $n = 15$ retinas; $P = 0.0069$) (d) and hydroxyproline residues (WT, $n = 15$ retinas; *Vldlr*^{-/-}, $n = 12$ retinas, $P = 0.0004$) (e) in WT and *Vldlr*^{-/-} retinas, as measured by LC-MS/MS. (f) Representative immunoblots (left) and quantification (right) of Hif1 α protein levels in nuclear lysates from retinas of WT, *Vldlr*^{-/-} and *Vldlr*^{-/-} *Ffar1*^{-/-} mice ($n = 3$ retinas per group). Fibrillar (Fbl) was used as a loading control for nuclear proteins. Cell lysates from $CoCl_2$ -treated or PBS-treated RAW264.7 (macrophage) cells were used as positive (+) and negative (-) controls, respectively. (g) Representative flat-mount (left) and extended-focus 3D confocal (middle and right) images (of $n = 3$ retinas per group) of Hif1 α expression (green) in the photoreceptor layer of retinas from P12 *Vldlr*^{-/-} mice. Lectin (red) stains for blood vessels, and blue opsin (blue) stains for cone photoreceptors. Scale bars, 100 μ m (left) and 30 μ m (middle and right). (h) Vegfa concentrations in the retinas of P16 mice of the indicated genotypes, as determined by ELISA ($n = 6$ retinas per group). (i) Representative flat-mount (left) and extended-focus 3D confocal (middle and right) images (of $n = 3$ retinas per group) of Vegfa expression in retinas of P16 *Vldlr*^{-/-} mice. Scale bars, 100 μ m (all panels). (j) Levels of VEGFA, as determined by ELISA, in the vitreous of human subjects with AMD (either those with RAP ($n = 3$) or CNV ($n = 7$) or in control subjects without pathologic neovessels (Ctl; with macular hole, $n = 8$). Results are presented as mean \pm s.e.m. * $P < 0.05$, ** $P < 0.01$, *** $P < 0.001$; by two-tailed Student's *t*-test (c,d), Mann-Whitney *U* test (b,e) or one-way ANOVA with *post hoc* Dunnett's (f,j) or Tukey's multiple comparison (h).



levels) and α -KG (Fig. 4b–d). Together with oxygen, α -KG is a necessary co-activator of prolyl-hydroxylase dehydrogenase (PHD), the enzyme that tags Hif1 α for degradation by proline hydroxylation³¹. A decreased level of hydroxyproline was detected in *Vldlr*^{-/-} retinas as compared to WT retinas (Fig. 4e), consistent with reduced PHD activity. Indeed, the reduction in retinal glucose uptake in 661W photoreceptor cells that was induced by GW9508 treatment or by glucose starvation was associated with Hif1 α stabilization (Supplementary Fig. 9a–c) and Vegfa secretion (Supplementary Fig. 9d,e). *In vivo*, Hif1 α stabilization in *Vldlr*^{-/-} photoreceptors (Fig. 4f,g) was associated with increased Vegfa production (Fig. 4h,i). Concurrent *Ffar1* and *Vldlr* deficiency reversed this effect and decreased Hif1 α and Vegfa levels (Fig. 4f,h), which was associated with fewer vascular lesions (Fig. 3i).

Increased expression of Vegfa from photoreceptors is sufficient to promote RAP-like lesions. Mice engineered to secrete Vegfa in photoreceptors develop RAP comparable to that in *Vldlr*^{-/-} mice³².

There may be other mechanisms of Hif1 α stabilization. Notably, the oxidative stress associated with an energy crisis may directly stabilize Hif1 α and promote Vegfa secretion from *Vldlr*^{-/-} photoreceptors^{4,33,34}, potentially contributing to vascular lesion formation. Although macrophages are often implicated in the etiology of AMD, we did not find evidence for their association with the onset of nascent RAP-like lesion development in retinas from *Vldlr*^{-/-} mice; we also observed that macrophages surrounded mature but not immature vascular lesions (Supplementary Fig. 10). To translate these findings to human disease, we measured vitreous VEGFA levels in human subjects with AMD, who had choroidal neovascularization (CNV) or RAP. These levels were higher than those in control subjects with a macular hole (i.e., without neovascularization) (Fig. 4j). These findings imply that an insufficiency of lipid and glucose fuels in the retina, in part through a reduction in the Krebs cycle metabolite α -KG, can drive aberrant angiogenesis in the normally avascular photoreceptor layer.

In the retina, the ability to use both lipids and glucose as fuel might be beneficial in periods of high fuel need or fuel deprivation. Fasting liberates fatty acid from adipose tissue, which is used by high-energy-consuming organs capable of fatty acid β -oxidation, such as the heart and perhaps the retina. Indeed, disorders of fatty acid β -oxidation are associated with retinopathy³⁵. Moreover, Ppara agonists that increase fatty acid β -oxidation have been used successfully to prevent diabetic proliferative retinopathy³⁶, and further exploration of the role of Ppara in metabolic signaling in neovascular eye disease is warranted. Overall, our findings suggest that lipids are an energy substrate in the retina, challenging the current dogma that glucose is the only fuel for photoreceptors.

Tissues that use lipid as fuel curb glucose uptake during starvation^{1,37}; thus, the capacity to sense nutrient availability and adapt fuel uptake accordingly might improve metabolic efficiency. GPCRs are known membrane sensors for the availability of amino acids, glucose and lipids³⁸. Here we show that Ffar1 is a metabolic sensor of fatty acid availability, which controls glucose entry into the retina. We speculate that long-term suppression of glucose entry by Ffar1 in photoreceptors (perhaps secondary to increased levels of circulating lipids) might contribute to age-related mitochondrial dysfunction in AMD or MacTel. The retinal effects of Ffar1 agonists, which are currently being considered for the treatment of type 2 diabetes, should be carefully monitored, particularly in older individuals who are at an increased risk for AMD.

Dysregulated mitochondrial metabolism might contribute to pathological angiogenesis in other diseases, such as cancer. Viewed in this context, the Warburg effect—in which suppressed mitochondrial oxidative phosphorylation leads to lower levels of α -KG—promotes angiogenesis at the cost of efficient ATP production^{31,39,40}. Decreased levels of α -KG would decrease PHD activity, leading to Hif1a stabilization, which would drive tumor angiogenesis. Our findings suggest the importance of mitochondrial fuel starvation as a driver of angiogenesis, matching energy demands with vascular supply. With a decline in mitochondrial function with age, this process may contribute to pathological angiogenesis in diseases associated with aging retina.

In summary, we show that lipid uptake and lipid β -oxidation are curtailed in *Vldlr*^{-/-} retinas. Increased levels of circulating fatty acids can activate Ffar1, leading to decreased retinal glucose uptake and decreased levels of the Krebs cycle intermediate α -KG. Consequently, Hif1a is stabilized and Vegfa is secreted by *Vldlr*^{-/-} photoreceptors, giving rise to pathologic RAP-like neovessels. This study highlights three new mechanistic insights into retinal physiology and neovascular AMD–RAP: (i) lipid β -oxidation is an energy source for the retina; (ii) Ffar1 is an important nutrient sensor of circulating lipids that controls retinal glucose entry to match mitochondrial metabolism with the available fuel substrates; and (iii) nutrient scarcity is a driver of pathological angiogenesis in the retina. These insights may thus contribute to the discovery of new treatments for retinal disease.

METHODS

Methods and any associated references are available in the [online version of the paper](#).

Accession codes. Gene Expression Omnibus: Microarray data have been deposited under accession code [GSE78831](#).

Note: Any Supplementary Information and Source Data files are available in the [online version of the paper](#).

ACKNOWLEDGMENTS

This work was supported by the US National Institutes of Health (NIH) grants EY024864 (L.E.H.S.), EY017017 (L.E.H.S.), EY022275 (L.E.H.S.), P01 HD18655 (L.E.H.S.) and EY024963 (J.C.), the Lowy Medical Research Institute (L.E.H.S.), the European Commission FP7 project 305485 PREVENT-ROP (L.E.H.S.), a Burroughs Wellcome Fund Career Award for Medical Scientists (J.-S.J.), the Foundation Fighting Blindness (J.-S.J.), the Canadian Institute of Health Research (CIHR) grant 143077 (J.-S.J.), the Fonds de Recherche du Québec–Santé (FRQS) (J.-S.J.), the Canadian Child Health Clinician Scientist Program (J.-S.J.), a CIHR New Investigator Award (J.-S.J.), the Knights Templar Eye Foundation (Z.F.), the Bernadotte Foundation (Z.F.), the Canada Research chair and CIHR grant 221478 (P.S.), the Boston Children's Hospital Ophthalmology Foundation (J.C.), a Boston Children's Hospital Faculty Career Development Award (J.C.), the Bright Focus Foundation (J.C.) and the Massachusetts Lions Eye Research Fund, Inc. (J.C.). We thank M. Puder and P. Nandivada (Harvard Medical School, Boston Children's Hospital) for sharing the *Ffar1*^{-/-} mice; M. Al-Ubaidi (University of Oklahoma) for sharing the 661W photoreceptor cells; Z. Lin and W.T. Pu (Harvard Medical School, Boston Children's Hospital) for sharing a modified CAG-GFP-miR30 construct; and C. Cepko (Harvard Medical School) and T. Li (National Eye Institute) for providing the pAAV-RK-GFP vector.

AUTHOR CONTRIBUTIONS

J.-S.J. and L.E.H.S. conceived and designed all experiments, and wrote the manuscript; and J.-S.J., Y.S., Z.S., L.P.E., N.S., T.F., S.B., J.S.K., G.P., A.M.J., C.G.H., C.J.H., Z.C. and Z.F. performed all *in vivo* and *ex vivo* experiments, except for those indicated below. M.L.G., E.A. and M. Friedlander performed and analyzed the Seahorse experiments; K.A.P. and C.B.C. performed and analyzed the metabolite profiling; P.B. and B.M. performed and analyzed fatty acid β -oxidation; M.B.P., K.V. and M. Fruttiger performed and analyzed 3D SEM; M.B. and E.L. analyzed lipid composition of plasma; F.A.R. collected human vitreous samples; P.S. measured human vitreous VEGF levels; C.B.C., M. Friedlander, J.C., P.S., B.M., F.A.R., A.P., M. Fruttiger and E.L. provided expert advice. All of the authors analyzed the data.

COMPETING FINANCIAL INTERESTS

The authors declare no competing financial interests.

Reprints and permissions information is available online at <http://www.nature.com/reprints/index.html>.

- Cahill, G.F. Jr. Starvation in man. *N. Engl. J. Med.* **282**, 668–675 (1970).
- Wong-Riley, M.T.T. Energy metabolism of the visual system. *Eye Brain* **2**, 99–116 (2010).
- Cohen, L.H. & Noell, W.K. Glucose catabolism of rabbit retina before and after development of visual function. *J. Neurochem.* **5**, 253–276 (1960).
- Dorrell, M.I. *et al.* Antioxidant or neurotrophic factor treatment preserves function in a mouse model of neovascularization-associated oxidative stress. *J. Clin. Invest.* **119**, 611–623 (2009).
- Niu, Y.-G. & Evans, R.D. Very-low-density lipoprotein: complex particles in cardiac energy metabolism. *J. Lipids* **2011**, 189876 (2011).
- Goudriaan, J.R. *et al.* The VLDL receptor plays a major role in chylomicron metabolism by enhancing LPL-mediated triglyceride hydrolysis. *J. Lipid Res.* **45**, 1475–1481 (2004).
- Bottoni, F. *et al.* Treatment of retinal angiomatous proliferation in age-related macular degeneration: a series of 104 cases of retinal angiomatous proliferation. *Arch. Ophthalmol.* **123**, 1644–1650 (2005).
- Yannuzzi, L.A. *et al.* Idiopathic macular telangiectasia. 2006. *Retina* **32** (suppl. 1), 450–460 (2012).
- Lim, L.S., Mitchell, P., Seddon, J.M., Holz, F.G. & Wong, T.Y. Age-related macular degeneration. *Lancet* **379**, 1728–1738 (2012).
- Okawa, H., Sampath, A.P., Laughlin, S.B. & Fain, G.L. ATP consumption by mammalian rod photoreceptors in darkness and in light. *Curr. Biol.* **18**, 1917–1921 (2008).
- Mantych, G.J., Hageman, G.S. & Devaskar, S.U. Characterization of glucose transporter isoforms in the adult and developing human eye. *Endocrinology* **133**, 600–607 (1993).
- Gospe, S.M. III, Baker, S.A. & Arshavsky, V.Y. Facilitative glucose transporter Glut1 is actively excluded from rod outer segments. *J. Cell Sci.* **123**, 3639–3644 (2010).
- Klepper, J. Glucose transporter deficiency syndrome (GLUT1DS) and the ketogenic diet. *Epilepsia* **49** (suppl. 8), 46–49 (2008).
- Lopaschuk, G.D., Ussher, J.R., Folmes, C.D.L., Jaswal, J.S. & Stanley, W.C. Myocardial fatty acid metabolism in health and disease. *Physiol. Rev.* **90**, 207–258 (2010).
- Obunike, J.C. *et al.* Transcytosis of lipoprotein lipase across cultured endothelial cells requires both heparan sulfate proteoglycans and the very-low-density lipoprotein receptor. *J. Biol. Chem.* **276**, 8934–8941 (2001).

16. Tyni, T., Paetau, A., Strauss, A.W., Middleton, B. & Kivelä, T. Mitochondrial fatty acid β -oxidation in the human eye and brain: implications for the retinopathy of long-chain 3-hydroxyacyl-CoA dehydrogenase deficiency. *Pediatr. Res.* **56**, 744–750 (2004).
17. Sarac, O., Gulsuner, S., Yildiz-Tasci, Y., Ozcelik, T. & Kansu, T. Neuro-ophthalmologic findings in humans with quadrupedal locomotion. *Ophthalmic Genet.* **33**, 249–252 (2012).
18. Trick, G.L. & Berkowitz, B.A. Retinal oxygenation response and retinopathy. *Prog. Retin. Eye Res.* **24**, 259–274 (2005).
19. Furukawa, T., Morrow, E.M. & Cepko, C.L. *Crx*, a novel Otx-like homeobox gene, shows photoreceptor-specific expression and regulates photoreceptor differentiation. *Cell* **91**, 531–541 (1997).
20. Winkler, B.S. Glycolytic and oxidative metabolism in relation to retinal function. *J. Gen. Physiol.* **77**, 667–692 (1981).
21. Hu, W. *et al.* Expression of VLDLR in the retina and evolution of subretinal neovascularization in the knockout-mouse model's retinal angiomatous proliferation. *Invest. Ophthalmol. Vis. Sci.* **49**, 407–415 (2008).
22. Lefebvre, P., Chinetti, G., Fruchart, J.-C. & Staels, B. Sorting out the roles of PPAR- α in energy metabolism and vascular homeostasis. *J. Clin. Invest.* **116**, 571–580 (2006).
23. Nakamura, M.T., Yudell, B.E. & Loor, J.J. Regulation of energy metabolism by long-chain fatty acids. *Prog. Lipid Res.* **53**, 124–144 (2014).
24. Itoh, Y. *et al.* Free fatty acids regulate insulin secretion from pancreatic beta cells through GPR40. *Nature* **422**, 173–176 (2003).
25. Kebede, M. *et al.* The fatty acid receptor GPR40 plays a role in insulin secretion *in vivo* after high-fat feeding. *Diabetes* **57**, 2432–2437 (2008).
26. Alquier, T. *et al.* Deletion of *Gpr40* impairs glucose-induced insulin secretion *in vivo* in mice without affecting intracellular fuel metabolism in islets. *Diabetes* **58**, 2607–2615 (2009).
27. Steneberg, P., Rubins, N., Bartoov-Shifman, R., Walker, M.D. & Edlund, H. The FFA receptor GPR40 links hyperinsulinemia, hepatic steatosis and impaired glucose homeostasis in mouse. *Cell Metab.* **1**, 245–258 (2005).
28. Honoré, J.-C. *et al.* Fatty acid receptor Gpr40 mediates neuromicrovascular degeneration induced by transarachidonic acids in rodents. *Arterioscler. Thromb. Vasc. Biol.* **33**, 954–961 (2013).
29. Briscoe, C.P. *et al.* The orphan G protein-coupled receptor GPR40 is activated by medium- and long-chain fatty acids. *J. Biol. Chem.* **278**, 11303–11311 (2003).
30. Naik, H. *et al.* Safety, tolerability, pharmacokinetics and pharmacodynamic properties of the GPR40 agonist TAK-875: results from a double-blind, placebo-controlled single-oral-dose rising study in healthy volunteers. *J. Clin. Pharmacol.* **52**, 1007–1016 (2012).
31. Kaelin, W.G. Jr. Cancer and altered metabolism: potential importance of hypoxia-inducible factor and 2-oxoglutarate-dependent dioxygenases. *Cold Spring Harb. Symp. Quant. Biol.* **76**, 335–345 (2011).
32. Ohno-Matsui, K. *et al.* Inducible expression of vascular endothelial growth factor in adult mice causes severe proliferative retinopathy and retinal detachment. *Am. J. Pathol.* **160**, 711–719 (2002).
33. Zhou, X., Wong, L.L., Karakoti, A.S., Seal, S. & McGinnis, J.F. Nanoceria inhibit the development and promote the regression of pathologic retinal neovascularization in the *Vldlr*-knockout mouse. *PLoS One* **6**, e16733 (2011).
34. Chen, Y. *et al.* Photoreceptor degeneration and retinal inflammation induced by very-low-density lipoprotein receptor deficiency. *Microvasc. Res.* **78**, 119–127 (2009).
35. Fletcher, A.L., Pennesi, M.E., Harding, C.O., Weleber, R.G. & Gillingham, M.B. Observations regarding retinopathy in mitochondrial trifunctional protein deficiencies. *Mol. Genet. Metab.* **106**, 18–24 (2012).
36. Keech, A.C. *et al.* Effect of fenofibrate on the need for laser treatment for diabetic retinopathy (FIELD study): a randomized controlled trial. *Lancet* **370**, 1687–1697 (2007).
37. Ferrannini, E., Barrett, E.J., Bevilacqua, S. & DeFronzo, R.A. Effect of fatty acids on glucose production and utilization in man. *J. Clin. Invest.* **72**, 1737–1747 (1983).
38. Wauson, E.M., Lorente-Rodríguez, A. & Cobb, M.H. Minireview: nutrient sensing by G protein-coupled receptors. *Mol. Endocrinol.* **27**, 1188–1197 (2013).
39. Warburg, O. On the origin of cancer cells. *Science* **123**, 309–314 (1956).
40. Zhao, S. *et al.* Glioma-derived mutations in *IDH1* dominantly inhibit *IDH1* catalytic activity and induce HIF-1 α . *Science* **324**, 261–265 (2009).



ONLINE METHODS

Mice. All studies adhered to the NIH Guide for the Care and Use of Laboratory Animals⁴¹ and the Association for Research in Vision and Ophthalmology (ARVO) Statement for the Use of Animals in Ophthalmic and Vision Research (http://www.arvo.org/About_ARVO/Policies/Statement_for_the_Use_of_Animals_in_Ophthalmic_and_Visual_Research/) and were approved by the Institutional Animal Care and Use Committee at Boston Children's Hospital. *Vldlr*-knockout mice (*Vldlr*^{-/-}; Jackson Lab stock: 002529) were crossed with wild-type C57BL/6 mice to obtain heterozygous breeders for littermate-controlled experiments. *Vldlr*^{-/-} mice were also crossed with *Ffar1*-knockout (*Ffar1*^{-/-}) mice¹ to ultimately obtain *Vldlr*^{-/-}*Ffar1*^{-/-} heterozygous breeders and double-knockout mice (*Vldlr*^{-/-}*Ffar1*^{-/-}). Pups weighing <5 g or >7 g at postnatal day (P)16 were excluded⁴². Littermate *Vldlr*^{-/-} pups were treated from P8 to P15 with WY164363 (50 mg per kg body weight (mg/kg) once daily; by intraperitoneal injection (i.p.); Sigma), GW9508 (14 μM, once daily; i.p.; Cayman), TAK-875 (15 mg/kg twice daily; by gavage; Selleckchem), medium-chain triglyceride oil (MCT; 20 μl once daily; by gavage; Nestle) or the corresponding vehicle and were sacrificed at P16 to quantify retinal vascular lesions. Mouse pups of both genders were used.

Quantification of vascular lesions. For quantification of outer retina vascular lesions, which are reminiscent of retinal angiomatous proliferation (RAP) or macular telangiectasia (MacTel), mice were euthanized with a mixture of xylazine and ketamine. Eyes were enucleated and fixed in 4% paraformaldehyde for 1 h at room temperature. Retinas were dissected, all hyaloid vessels were carefully removed, and the retinas were stained overnight at room temperature with fluoresceinated isolectin B₄ (lectin) (Alexa Fluor 594 – I21413, Molecular Probes) in 1 mM CaCl₂ in PBS. Lectin-stained retinas were whole-mounted onto Superfrost/Plus microscope slides (Fisher Scientific) with the photoreceptor side up and embedded in SlowFade Antifade reagent (Invitrogen). For quantification of retinal lesions, 20 images of each whole-mounted retina were obtained at 10× magnification on a Zeiss AxioObserver.Z1 microscope and merged to form one image using AxioVision 4.6.3.0 software. Vascular lesion counts were analyzed using the SWIFT_MACTEL method, an adaptation of the method used to measure neovascularization (SWIFT_NV)⁴³ in the oxygen-induced retinopathy model.

SWIFT_MACTEL. We created a set of macros that was developed to run on the ImageJ platform (NIH; <http://imagej.nih.gov/ij/>). In brief, SWIFT_MACTEL isolates the red channel from a lectin-stained retinal whole mount, divides the image into four quadrants and removes background fluorescence to allow for the neovascularization (NV) structures to stand out clearly against the background fluorescence of normal vessels. Using a slide bar to either increase or decrease a particular quadrant's fluorescence threshold, the SWIFT_MACTEL user designates a threshold that marks NV structures but not normal vessels in each quadrant. After setting the appropriate threshold, artifacts like cellular debris or hyperfluorescent retinal edges can be manually removed and excluded from quantification. SWIFT_MACTEL then analyzes all pixels in the image that lie above the chosen intensity threshold and that are part of an object that has a minimum size of 100 pixels. By setting this cut-off in object size, small artifacts like vessel branch points are automatically removed. After measuring all four quadrants, SWIFT_MACTEL creates a composite from all four NV quadrants and calculates the total NV pixel number. Results from the SWIFT_NV method have been found to correlate well with results from the established hand-measurement-based protocols ($R^2 = 0.9372$) and show robust intra-individual ($R^2 = 0.9376$) and inter-individual ($R^2 = 0.9424$) reproducibility⁴². The *n* number is the number of eyes quantified.

Scanning electron microscopy and three-dimensional (3D) retinal reconstruction. Tissue was processed for serial block-face scanning electron microscopy (SEM) using an adapted version of a protocol established by Deerinck *et al.* 2010 (ref. 44). Whole eyes were isolated and fixed in Karnovsky's fixative. The cornea and lens were removed and the tissue was further fixed in tannic acid overnight. Heavy-metal infiltration was then undertaken; tissue was incubated in 1.5% potassium ferrocyanide and 0.5% osmium tetroxide

in cacodylate buffer, followed by thiocarbonylhydrazide treatment and a second exposure to 1% osmium. Walton's lead aspartate exposure was not carried out, so preparation of the tissue was finished with a 1% uranyl acetate incubation followed by dehydration to propylene oxide, and the tissue was embedded in Durcupan ACM resin. The tissue was serially sectioned and imaged using the Gatan 3VIEW serial block-face imaging system (Gatan, Abingdon, UK) fitted to a Zeiss Sigma variable pressure-field emission scanning electron microscope (Zeiss, Cambridge, UK). Data was collected and used in Amira Software (FEI, Oregon, USA) in order to reconstruct the 3D images. Using the same software, photoreceptor mitochondrial volume was estimated for WT mice, around the lesion in *Vldlr*^{-/-} mice, and away from the lesion in *Vldlr*^{-/-} mice.

ATP measurements. ATP was measured using a kit, as per the instruction manual (Molecular Probes, A22066). Briefly, a standard reaction solution was made from the following components: dH₂O, 20× Reaction Buffer, DTT (0.1 M), D-luciferin (10 mM), and firefly luciferase stock solution (5 mg/ml). Low-concentration ATP standard solutions were prepared by diluting ATP solution (5 mM) in dH₂O. A standard curve was generated by subtracting the background luminescence of the standard reaction solution from luminescence readings for a series of dilute ATP standard solutions. Luminescence measurements were taken for ATP-containing samples, and the amount of ATP in experimental samples was calculated from the standard curve.

Oxygen-consumption and extracellular-acidification rates. All oxygen-consumption rates (OCRs) were measured using a Seahorse XF⁹⁶ Flux Analyzer. Whole retinas were isolated and 1-mm punch biopsies were loaded into a 96-well plate. Retinal punches were incubated in assay medium (Dulbecco's modified Eagle's medium (DMEM) 5030 supplemented with 12 mM glucose, 10 mM HEPES and 26 mM NaHCO₃) to measure OCRs and extracellular acidification rates (ECARs). Photoreceptor (661W) cells were incubated in assay medium (DMEM 5030, 12 mM glucose, 10 mM HEPES) 1 hour before taking measurements. Fatty acid oxidation rates were determined by treating tissues or cells with etomoxir (40 μM; Sigma) 40 min before analysis and then providing BSA (control) or a BSA-palmitate conjugate (Seahorse). Glucose oxidation rates were measured after injection of 2-deoxyglucose (2-DG, 100 mM; Sigma) or a medium control during data acquisition. To determine the amount of proton uncoupling (OCR independent of ATP production), oligomycin (2 μM), an inhibitor of ATP synthase, was injected. To determine the maximal fatty acid or glucose oxidative capacity, the nonmitochondrial respiration rate (measured after injection of 2 μM rotenone and 2 μM antimycin A (RAA)) was subtracted from the oxygen-consumption rate measured after injection of 0.5 μM carbonyl cyanide-*p*-trifluoromethoxyphenylhydrazone (FCCP).

Glucose and lactate measurements. Whole retinas and photoreceptors (661W) were incubated in assay medium (DMEM 5030, 12 mM glucose, 10 mM HEPES) for 6 and 48 h, respectively. Medium was collected and spun briefly (13,000g) to remove cellular debris, and glucose and lactate levels measured using a Yellow Springs Instrument (YSI) 2950; results were compared to control medium that was not exposed to tissue or cells. To determine the conversion of glucose to lactate (the glycolytic rate), the amount of lactate produced was divided by the amount of glucose taken up.

Retinal lipid uptake. We compared retinal uptake of long-chain fatty acid in wild-type and *Vldlr*^{-/-} mice gavaged with 0.1 mg of 4,4-difluoro-5,7-dimethyl-4-bora-3a, 4a-diaza-*s*-indacene-3-hexadecanoic acid (BODIPY FL C16; Molecular Probes). Mice were euthanized 2 h later, and the eyes were enucleated, embedded in OCT and cryosectioned (10 μm) for immediate imaging by fluorescence microscopy. Retinal fatty acid uptake was quantitated using a ¹⁴C-labeled 2-bromopalmitate tracer injected twice daily (i.p.; 0.5 μCi per dose) from P9 to P12; the total administered radioactivity was normalized for mouse body weight. Retinas were then dissected and homogenized in Ultima Gold liquid scintillation cocktail (PerkinElmer) and beta-counted (¹⁴C disintegration per minute or DPM) using a Tri-Carb 2900TR instrument (PerkinElmer), correcting for background scintillation.

Plasma triglycerides and fatty acid analysis. Plasma was isolated from WT and *Vldlr*^{-/-} mice by centrifugation (2000g × 20 min; 4 °C) of whole blood in EDTA-coated tubes. Triglycerides were determined using the RANDOX TRIGS kit (TR210), according to the manufacturer's instructions. Fatty acids in whole plasma were assayed as described previously⁴⁵. Briefly, each sample was subjected to direct trans-esterification and then injected into a gas chromatograph using the Agilent GC AutoSampler system (7890A). Fatty acids were identified by comparison with the expected retention times of known standards and then analyzed with the OpenLAB Software Suite (Agilent).

β-oxidation metabolite quantification. Acylcarnitine metabolites were extracted from WT and *Vldlr*^{-/-} (P12) flash-frozen retinas using ice-cold methanol. Samples were sonicated and centrifuged, and the supernatant was transferred to a fresh tube for nitrogen evaporation. After drying, butanolysis was performed (butanol-HCl, 55 °C for 20 min) before reconstitution in mobile phase (acetonitrile (ACN):H₂O 80:20, formic acid 0.05%). Samples were analyzed by liquid chromatography followed by tandem mass spectrophotometry (LC-MS/MS, Alliance 2795 LC and Quattro Micro, Waters Corp.). Data were recorded in positive-electrospray ionization mode and analyzed with Neolynx software (Waters Corp.).

Retinal glucose uptake. Positron emission tomography (PET) imaging studies were performed on WT, *Vldlr*^{-/-}, *Vldlr*^{-/-}*Ffar1*^{-/-} and *Ffar1*^{-/-} mice (P16; Focus 120 high-resolution; Siemens), followed by micro-computerized axial tomography (microCAT) scan imaging (MicroCAT II scanner, Siemens). Fluorine-18 fluorodeoxyglucose ([¹⁸F]FDG) was administered by intraperitoneal injection to obtain nontoxic radioactivity levels (3.7 and 37 MBq; or 0.1 to 1.0 mCi). Actual administered activity was determined using a dose calibrator to measure activity in the syringe before and after the injection. Images were acquired 60 min after injection to ensure radiotracer uptake. Mice were fasted for 6 h before imaging, kept in darkness and anesthetized by inhalation of isoflurane (2–4%) through a nose cone for the duration of the procedure. Animals were imaged in a head first, prone position and placed on a heating pad to maintain appropriate body temperature. Upon completion of imaging, mice were euthanized and retinas were dissected for precise [¹⁸F]FDG retinal activity, quantification by gamma counter, and correction for decay. WT and *Vldlr*^{-/-} mouse pups were also injected with trace amounts of 2-[³H]deoxyglucose (0.5 μCi daily, i.p.) and treated with GW9508 or vehicle (14 μM daily, i.p.) for 5 d (P7–P12). Retinas were collected and homogenized in a scintillation cocktail (Ecolite +; MP Biomedicals), and beta counts were measured using a LS6500 Multipurpose Scintillation Counter (Beckman).

Laser-capture microdissection. Eyes were embedded in OCT and flash-frozen immediately following enucleation. Eyes were cryosectioned under RNase-free conditions into 10-μm-thick sections, and collected on RNase-free polyethylene naphthalate glass slides (11505189, Leica). Sections were stained for lectin (1:50 in 1 mM CaCl₂) and dehydrated with 70%, 90% and 100% ethanol washes. Retinal vessels and layers were microdissected with a Leica LMD 6000 system (Leica Microsystems) and collected directly into RNA-stabilizing buffer from the RNeasy Micro kit (Qiagen, Chatsworth, CA). RNA was extracted from microdissected tissues using the RNeasy kit as described above (Qiagen), and real-time PCR was performed with the generated cDNA.

Reverse transcription and quantitative real-time PCR analysis. RNA samples from cell culture, whole retina or laser-captured neovessels and layers were treated with DNase I (Qiagen, Chatsworth, CA) to remove any contaminating genomic DNA. The DNase-treated RNA was then converted into cDNA using reverse transcriptase (Invitrogen). PCR primers (Supplementary Table 1) for target genes and the control gene, peptidylprolyl isomerase A (*Ppia*; which encodes cyclophilin A), were designed using Primer Bank and NCBI Primer Blast software. Quantitative analysis of gene expression was generated using an ABI Prism 7700 Sequence Detection System with the SYBR Green Master mix kit, and gene expression was calculated relative to that of *Ppia* using the ΔC_T method.

Expression array. Illumina mouse gene-microarray analysis of WT and *Vldlr*^{-/-} retinas was performed in biological triplicate (Mouse-WG6 expression

BeadChip, Illumina). The chip contains 45,000 probe sets representing 34,000 genes. Microarray studies, from cDNA synthesis to raw data normalization, were performed by the Molecular Genetics Core Facility at Boston Children's Hospital. Briefly, total RNA (1 μg each) was reverse-transcribed, followed by a single *in vitro* transcription amplification to incorporate biotin-labeled nucleotide, and subsequent hybridization and staining with streptavidin-Cy3 was performed according to the manufacturer's instructions. The chip was scanned with an Illumina BeadArray Reader to measure the signal intensity of the labeled target. Raw data were analyzed with microarray software (Bead Studio Gene Expression version 3.4.0) for quality control, background analysis and normalization with the rank-invariant algorithm. Normalized data was further analyzed for comparative molecular and cellular pathway regulation using Ingenuity Pathway Analysis (*P* = 0.05 and delta of 0.19; Qiagen)⁴⁶.

Immunohistochemistry. For whole-mount immunohistochemistry, eyes were enucleated and fixed in 4% paraformaldehyde at room temperature for 1 h. The retina was isolated and stained for retinal vasculature and lesions with fluoresceinated isolectin B4 (Alexa Fluor 594 in PBS with 1 mM CaCl₂; I21413, Molecular Probes) overnight at room temperature (RT). Retinas were visualized using a 5× objective with a Zeiss AxioObserver.Z1 microscope and imaged with a Zeiss AxioCam MRm operated by AxioVision software (version 4.6.3.0). Whole mounts were also fixed and permeabilized in cold methanol (20 min at -20 °C), blocked in 3% bovine serum albumin and 0.1% Triton X-100, and stained with isolectin B₄ to visualize vessels (as above) and/or with primary antibodies against Hif1a (1:100 in TBS, NB00-134, Novus), VEGF (1:100, RB-222, Thermo Scientific), IBA-1 (1:200, CP290A, Biocare Medical UK) and blue opsin cone (1:100, sc-14365, Santa Cruz) overnight at 4 °C, followed by secondary antibody staining (1 h at RT; AlexaFluor 1:1,000, Invitrogen). Flat-mounts (and cross-sections) were imaged with confocal microscopy (Leica TCS SP2 AOBS) and z-stacks were 3D-reconstructed using Volocity software (PerkinElmer).

Immunoblotting and enzyme-linked immunosorbent assay (ELISA). Retinal samples were obtained as described above. Retinal lysate (20 μg) from three different animals or endothelial cell lysate (10 μg) was loaded on an SDS-PAGE gel and electroblotted onto a polyvinylidene difluoride (PVDF) membrane (Bio-Rad). We used retinal nuclear extract (Abcam, Ab113474) to enrich Hif1a signals, according to the manufacturer's instructions. After blocking, the membranes were incubated with antibodies against β-actin (Sigma, A1978), fibrillarlin (Cell Signaling, 2639), Hif1a (Novus, NB100-134), and Glut1 (Novus, NB300-666 and Abcam, Ab652), Glut3 (Millipore, AB1344) and Glut4 (Abcam, ab654) overnight (1:1,000 each). After washing, membranes were incubated with 1:10,000 horseradish peroxidase-conjugated anti-rabbit or anti-mouse secondary antibodies (Amersham, NA931V and NA934V) for 1 hour at room temperature. Densitometry was analyzed using ImageJ software. Retinal Vegfa concentration was measured by ELISA (MMV00, R&D Systems) according to the manufacturer's instructions and normalized to the total cellular protein content of each sample, as assessed by the bicinchoninic acid (BCA) assay (Thermo Fisher Scientific).

Metabolite profiling. Metabolites of rapidly dissected WT and *Vldlr*^{-/-} retinas (flash-frozen less than 1 min after euthanasia; 15 or 16 biological replicates) were homogenized in 80% methanol (8 μl/mg of tissue) containing the internal standards inosine[¹⁵N₄], thymine-d₄, and glycocholate-d₄ (Cambridge Isotope Laboratories) using a TissueLyser II (Qiagen) bead mill for 4 min at 20 Hz. Samples were centrifuged (9,000g, 10 min, 4 °C) to pellet debris, and supernatants were analyzed using two liquid chromatography tandem mass spectrometry (LC-MS/MS) methods to measure polar metabolites, as described previously^{47,48}. Briefly, negative-ionization mode multiple-reaction mode (MRM) data were acquired using an ACQUITY UPLC instrument (Waters) coupled to a 5500 QTRAP triple-quadrupole mass spectrometer (AB SCIEX). The supernatants were injected directly onto a 150 × 2.0 mm Luna NH2 column (Phenomenex) that was eluted at a flow rate of 400 μl/min with initial conditions of 10% mobile phase A (20 mM ammonium acetate and 20 mM ammonium hydroxide (Sigma-Aldrich) in water (VWR)) and 90% mobile phase B (10 mM ammonium hydroxide in 75:25 vol/vol acetonitrile/methanol

(VWR)) followed by a 10 min linear gradient to 100% mobile phase A. The ion spray voltage was -4.5 kV, and the source temperature was 500 °C. Positive-ionization mode MRM data were acquired using a 4000 QTRAP triple-quadrupole mass spectrometer (AB SCIEX) coupled to an 1100 Series pump (Agilent) and an HTS PAL autosampler (Leap Technologies). Cell extracts (10 μ l) were diluted using 40 μ l of 74.9:24.9:0.2 (vol/vol/vol) acetonitrile/methanol/formic acid containing stable isotope-labeled internal standards (0.2 ng/ μ l valine-d8, Isotec; and 0.2 ng/ μ l phenylalanine-d8 (Cambridge Isotope Laboratories)) and were injected onto a 150×2.1 mm Atlantis HILIC column (Waters). The column was eluted isocratically at a flow rate of 250 μ l/min with 5% mobile phase A (10 mM ammonium formate and 0.1% formic acid in water) for 1 min followed by a linear gradient to 40% mobile phase B (acetonitrile with 0.1% formic acid) over the course of 10 min. The ion spray voltage was 4.5 kV, and the source temperature was 450 °C. Raw data were processed using MultiQuant 2.1 (AB SCIEX) for automated peak integration, and metabolite peaks were manually reviewed for quality of integration and compared against known standards to confirm identity.

Photoreceptor (661W) cell culture. Cone photoreceptor cells^{49,50} were cultured as monolayers at 37 °C, 5% CO_2 in a humidified atmosphere in DMEM with FBS 10% supplemented with hydrocortisone (20 μ g/ 500 ml; H-2270, Sigma), progesterone (20 μ g/ 500 ml; P-8783, Sigma), putrescine (0.016 g/ 500 ml; P-7505, Sigma) and β -mercaptoethanol (20 μ l/ 500 ml; M-6250, Sigma). No mycoplasma contamination of the cells was detected. An equal number of 661W cells (0.3×10^6) was plated in each well of 6-well dishes and cultured to 80% confluence. Cells were washed twice with PBS, starved for 4 h (in the above-mentioned medium without FBS) and then stimulated with GW9508 (14 μ M, Cayman) or vehicle. Photoreceptors were collected 8 h after treatment to determine Hif1 α protein expression by immunoblotting, and conditioned medium was collected at 12 h to quantify Vegfa levels by ELISA (MMV00, R&D Systems) according to the manufacturer's instructions. Vegfa concentrations were normalized for the number of cells per well by measuring the total cellular protein content of each sample, as assessed by the BCA assay.

Preparation of AAV2-RK-shVldlr vector and AAV2 virus. Three shRNAs, each of which targets all eight variants of mouse *Vldlr*, were designed using a published algorithm⁵¹. DNA fragments were amplified, purified, digested and inserted into a modified CAG-GFP-miR30 vector according to a previous report⁵²; the synthetic CAG promoter (which includes the cytomegalovirus early enhancer element, the chicken *Actb* (which encodes β -actin) promoter and the splice acceptor of the rabbit beta1 globin gene) was replaced with the promoter of the gene encoding rhodopsin kinase (RK; encoded by *GRK1*) that was isolated from a pAAV-RK-GFP vector⁵³. *Vldlr* knockdown efficiency was tested in retinas from P0 C57BL/6 pups. Recombinant AAV2 vectors were produced as previously described⁵⁴. Briefly, the AAV vector, the replication-capsid packaging plasmid, and adenoviral helper plasmid were mixed with polyethylenimine and transfected into HEK293T cells (CRL-11268, American Type Culture Collection). Seventy-two hours after transfection, cells were harvested and the cell pellet was resuspended in virus buffer, followed by three cycles of freeze-thawing, and then homogenization. Cell debris was pelleted at $5,000$ g for 20 min, and the supernatant was run on an iodixanol gradient. Recovered AAV vectors were washed three times with PBS using Amicon 100K columns (EMD Millipore). Real-time PCR was used to determine genome titers of the recombinant AAV. This protocol was also used to prepare a control AAV2-shControl. Virus concentration of approximately 2×10^{12} genome copies per ml (gc/ml) was used for the experiments. The sequences ($5'$ - $3'$) of the mouse *Vldlr*-specific siRNAs

were as follows: shVldlr #1, GGAAAGTTCAAGTGCAGAAGCG; shVldlr #2, GGAATGCCATATCAACGAATGC; shVldlr #3, GGGATCTGCAGTCAAATT TGTA; Scramble shRNA control, GATTTAAGACAAGCGTATAACA.

Human samples and vitrectomy. The study conforms to the tenets of the Declaration of Helsinki, and approval of the human clinical protocol and informed consent were obtained from the Maisonneuve-Rosemont Hospital (HMR) ethics committee (ref. CER: 10059). All patients previously diagnosed with AMD or macular hole (without neovascularization, but requiring vitrectomy for treatment) were followed clinically, and surgery was performed, when indicated by 'standard-of-care' guidelines, by a single vitreoretinal surgeon (F.A.R.). Vitreous samples were frozen on dry ice immediately after biopsy and stored at -80 °C. VEGFA ELISAs were performed according to manufacturer's instructions (DVE00, R&D Systems).

Statistical analysis. We used Student's *t*-test, and ANOVA with Dunnett, Bonferroni or Tukey *post hoc* analysis (see **Supplementary Table 2**) to compare different groups; $P < 0.05$ was considered as statistically significant. The D'Agostino-Pearson or Kolmogorov-Smirnov (KS) normality test was used to confirm a normal distribution. Data with non-Gaussian distribution was analyzed using a Mann Whitney *U* test (nonparametric, two groups). Animals were not randomized, but quantification of the data was performed in a blinded fashion when possible. All experiments were repeated at least three times. Values >2 s.d. from the mean were considered to be outliers and were excluded. Sample size was estimated to detect a difference of 20% with a power of 80% ($1 - \beta$) and an α of 0.05 . Results are presented as mean \pm s.e.m. * $P < 0.05$, ** $P < 0.01$, *** $P < 0.001$.

- Committee for the Update of the Guide for the Care and Use of Laboratory Animals. *Guide for the Care and Use of Laboratory Animals* 8th edn. (The National Academies Press, Washington, D.C., 2011).
- Stahl, A. *et al.* Postnatal weight gain modifies severity and functional outcome of oxygen-induced proliferative retinopathy. *Am. J. Pathol.* **177**, 2715–2723 (2010).
- Stahl, A. *et al.* Computer-aided quantification of retinal neovascularization. *Angiogenesis* **12**, 297–301 (2009).
- Deerinck, T.J. *et al.* Enhancing serial block-face scanning electron microscopy to enable high-resolution 3D nanohistology of cells and tissues. *Microsc. Microanal.* **16**, 1138–1139 (2010).
- Spahis, S. *et al.* Plasma fatty acid composition in French-Canadian children with non-alcoholic fatty liver disease: effect of *n*-3 PUFA supplementation. *Prostaglandins Leukot. Essent. Fatty Acids* **99**, 25–34 (2015).
- Calvano, S.E. *et al.* A network-based analysis of systemic inflammation in humans. *Nature* **437**, 1032–1037 (2005).
- Jain, M. *et al.* Metabolite profiling identifies a key role for glycine in rapid cancer cell proliferation. *Science* **336**, 1040–1044 (2012).
- Townsend, M.K. *et al.* Reproducibility of metabolomic profiles among men and women in two large cohort studies. *Clin. Chem.* **59**, 1657–1667 (2013).
- al-Ubaidi, M.R. *et al.* Bilateral retinal and brain tumors in transgenic mice expressing simian virus 40 large T antigen under control of the human interphotoreceptor retinoid-binding protein promoter. *J. Cell Biol.* **119**, 1681–1687 (1992).
- Tan, E. *et al.* Expression of cone-photoreceptor-specific antigens in a cell line derived from retinal tumors in transgenic mice. *Invest. Ophthalmol. Vis. Sci.* **45**, 764–768 (2004).
- Park, Y.K. *et al.* AsiDesigner: exon-based siRNA design server considering alternative splicing. *Nucleic Acids Res.* **36**, W97–103 (2008).
- Grieger, J.C., Choi, V.W. & Samulski, R.J. Production and characterization of adeno-associated viral vectors. *Nat. Protoc.* **1**, 1412–1428 (2006).
- Khani, S.C. *et al.* AAV-mediated expression targeting of rod and cone photoreceptors with a human rhodopsin kinase promoter. *Invest. Ophthalmol. Vis. Sci.* **48**, 3954–3961 (2007).
- Vandenberghe, L.H. *et al.* Efficient serotype-dependent release of functional vector into the culture medium during adeno-associated virus manufacturing. *Hum. Gene Ther.* **21**, 1251–1257 (2010).